https://doi.org/10.5194/egusphere-2024-3210
Preprint. Discussion started: 18 October 2024

Observation and modelling of atmospheric OH and HO_2 radicals at a subtropical rural site and implications for secondary pollutants

Zhouxing Zou[1#], Tianshu Chen[1#], Qianjie Chen[1], Weihang Sun[1], Shichun Han[1], Zhuoyue Ren[2], Xinyi Li[2], Wei Song[2], Aoqi Ge[2], Qi Wang[2], Xiao Tian[2], Chenglei Pei[3], Xinming Wang[2], Yanli Zhang[2], and Tao Wang[1]

[#] These authors contributed equally to this work

[1] Department of Civil and Environmental Engineering, The Hong Kong Polytechnic University, Hong Kong, China

[2] Guangzhou Institute of Geochemistry, Chinese Academy of Sciences, Guangzhou, China

[3]Guangdong Province Guangzhou Ecological Environment Monitoring Center Station, Guangzhou 510030, China.

Correspondence to: Tao Wang (tao.wang@polyu.edu.hk)

Abstract

HO_X radicals (OH and HO_2) are crucial oxidants that determine atmospheric oxidation capacity and the production of secondary pollutants; however, their sources and sinks remain incompletely understood in certain forest and maritime environments. This study measured HO_2 and OH concentrations using a chemical ionisation mass spectrometer at a subtropical rural site in southern China from 12 November to 19 December 2022. The average peak concentrations were $3.50 \pm 2.47 \times 10^6$ cm^{-3} for OH and $1.34 \pm 0.93 \times 10^8$ cm^{-3} for HO_2. Calculations based on an observation-constrained chemical model revealed an overestimation of HO_2 and OH concentrations during warm periods of the field study. These inaccuracies resulted in overestimations of production rates in the model simulation by up to 98% for ozone and 341% for nitric acid. Our study highlights the need for further improving understanding of the sources/sinks of OH and HO_2.

1. Introduction

The HO_X family, comprising hydroxyl (OH) and peroxy radicals (HO_2), plays a pivotal role in the Earth's atmosphere by driving photochemical processes that influence the air composition and chemistry. OH radicals are primarily produced by the photolysis of ozone (O_3), nitrous acid (HONO), and ozonolysis of alkenes. They initiate the oxidation of CO and most volatile organic compounds (VOCs), producing HO_2 and other peroxyl radicals (RO_2, where R represents an alkyl group). HO_2 is also generated from the photolysis of oxygenated VOCs (OVOCs) and by reactions between OVOCs and OH. In the presence of NO, RO_2 radicals are converted to HO_2 and then to OH radicals buffering OH concentrations and maintaining atmospheric oxidation capacity. (Stone et al., 2012). These interactions are crucial in the formation of photochemical smog and secondary organic aerosol (SOA), which generate NO_2, O_3 and highly oxygenated molecules. HO_X radicals are removed through reactions of OH with inorganic trace gases, self-reactions among radicals, peroxyacetyl nitrate (PAN) formation, and the heterogeneous uptake by aerosols, subsequently contributing to atmospheric acidification and aerosol formation by the production of H_2SO_4 and HNO_3. See Text S1, Figure S1 and Table S1 for detailed processes and chemical reactions.

The accuracy of model-predicted OH is a crucial indicator for assessing our understanding of the atmosphere processes (Heard and Pilling, 2003). There is a longstanding debate regarding the discrepancies between simulated and observed radical concentrations under low NO_x condition which remains a significant issue (Hofzumahaus et al., 2009; Stone et al., 2012; Zou et al., 2023). Previous studies have shown that models generally predict OH levels well in polluted conditions (NO > 1 ppb), but notable overestimation were observed under low NO and aged conditions, such as coastal areas (Kanaya et al., 2007; Zou et al., 2023), marine boundary layers (Berresheim et al., 2002; Carslaw et al., 1999), and the Arctic region. Missing OH sinks were proposed as the primary reason for the overestimation (Lou et al., 2010; Yang et al., 2016; Hansen et al., 2014 Thames et al., 2020). Underestimation of OH concentrations were also observed in high biogenic VOCs (BVOCs) and low NO (<1 ppb) conditions (Hofzumahaus et al., 2009; Lelieveld et al., 2008; Tan et al., 2001;

https://doi.org/10.5194/egusphere-2024-3210
Preprint. Discussion started: 18 October 2024

Whalley et al., 2011). After considering a new OH regeneration mechanism (Wennberg et al., 2018; Novelli et al., 2020) and a measurement interference (Feiner et al., 2016; Hens et al., 2014; Mao et al., 2012; Novelli et al., 2014; Woodward-Massey et al., 2020), daytime OH concentration could be reasonably reproduced by the model in the high BVOC conditions, with some unresolved underestimation in the evening (Jeong et al., 2022; Lew et al., 2020; Tan et al., 2019).

HO_2 concentrations were consistently underpredicted in the polluted urban sites (Ma et al., 2019; Yang et al., 2021; Ma et al., 2022) and at a rural site (Tan et al., 2017), with no clear trends in relatively clean regions. Some studies reported good agreement between measurement and model prediction (Feiner et al., 2016; Lew et al., 2020), whereas others indicated model overprediction (Bottorff et al., 2023; Griffith et al., 2013) and underprediction (Kim et al., 2013; Mallik et al., 2018) . These discrepancies may be attributed to several factors, including: measurement interference caused by RO_2 recycling in environments rich in BVOCs or aromatics (Fuchs et al., 2011), uncertainties associated with heterogeneous uptake in box models (Yang et al., 2022), unmeasured sinks and the outflow of reservoir species like PAN (Griffith et al., 2013). Despite these advances, it remains difficult to pin down the exact causes of the model-measurement discrepancies in some of the previous studies.

In the present study, we measured concentrations of OH and HO_2 using a quadrupole chemical ionization mass spectrometer (PolyU-CIMS) from November to December 2022 at a subtropical rural site of southern China. We test model's capability in reproducing the radical concentrations and elucidate factors contributing to discrepancy under varying temperature, VOCs, and NO_X conditions. The Methodology section describes the measurement site, the principle and the configuration of PolyU-CIMS, and the setup of chemical box model. The Results and Discussion section details our findings, providing a comprehensive analysis of the radical concentrations and exploring the discrepancies between observed data and model predictions. By employing an observation-constrained box model, we analyzed the radical budgets and investigated potential causes for these discrepancies. The study concludes with a discussion of the implications of these findings.

2. Methodology

2.1 Measurement Site

The field campaign was conducted at the Conghua Liangkou Air Monitoring Station (23°44'47"N, 113°47'06"E, 200m, above sea level) from November 12 to December 19, 2022 (Figure 1). The site is located at the northern part of the Pearl River Delta (PRD), approximately 80 kilometers from the densely populated areas of the PRD and nestled within the Liuxi River National Forest Park (an evergreen broad-leaf forest). The site is situated just north of the G105 national highway and around 0.5 kilometer east from Liangkou town. Even though it is close to the road, the traffic was generally limited during the observation period due to the coronavirus disease pandemic (COVID 19). The site is subjected to the BVOC emission, predominantly isoprene, from the surrounding forest when the daytime temperature is exceeding 20°C, and NO emissions from the nearby national highway, particularly during periods of low wind speeds. The measurements comprised trace gases including O_3, NO, NO_2, CO, HONO, VOCs, OVOCs, meteorological data such as relative humidity (RH), temperature, and photolysis frequencies of HONO, NO_2, O_3, H_2O_2, and HCHO. Details about the instruments are shown in Table S2.

https://doi.org/10.5194/egusphere-2024-3210
Preprint. Discussion started: 18 October 2024

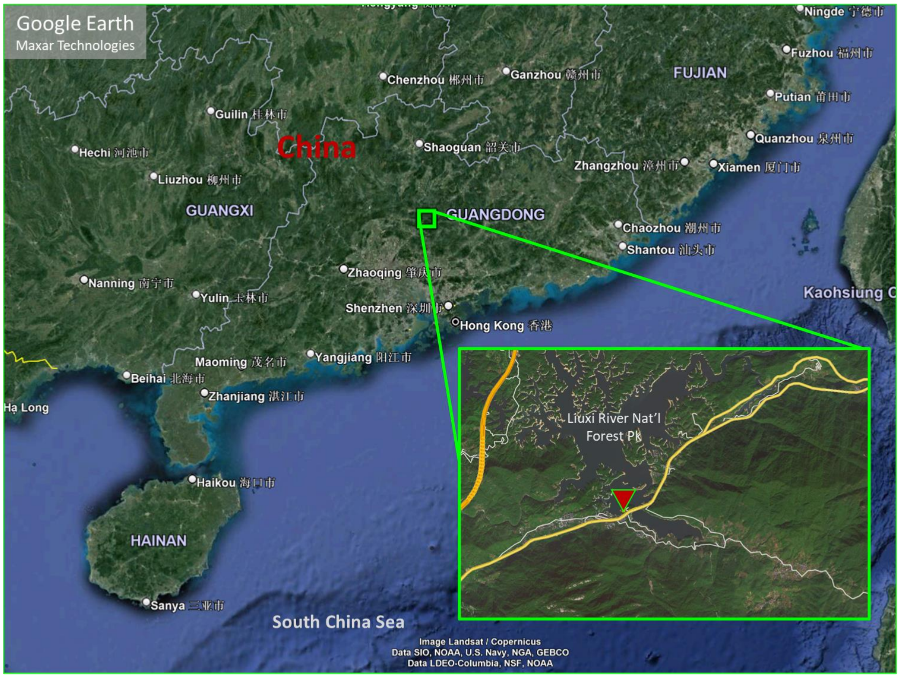

Figure 1 Geographic location of measurement site (Liangkou Air Monitoring station 23°44'47"N, 113°47'06"E, 200 m a.s.l. labelled by the red inverted triangle) in Conghua, Guangdong Province, South China. The map is sourced from © Google Earth and © Amap.

2.2 Radical measurement principle

OH and HO_2 radicals were measured using the Hong Kong Polytechnic University quadrupole Chemical Ionization Mass Spectrometer (PolyU-CIMS), which was used in a previous study (Zou et al., 2023) for OH measurement. The use of CIMS for OH measurement was pioneered by Eisele and Tanner, (1991), with subsequent enhancements in measurement accuracy (Eisele and Tanner, 1993; Tanner et al., 1997; Tanner and Eisele, 1995) and adoption of inlets for simultaneous measurements of HO_2 and RO_2 (Edwards et al., 2003; Sjostedt et al., 2007), H_2SO_4 (Mauldin III et al., 2004), and OH reactivity (Muller et al., 2018).

Figure 2 illustrates the measurement principle of the PolyU-CIMS used in this campaign. Briefly, the ambient OH radicals are converted to H_2SO_4 in the sample inlet system by reacting with SO_2 (R21 in the reaction Table S1) which is then transformed to HSO_4^- ion clusters in the ionization chamber by the reactions with a reagent gas in sheath flow (HNO_3, R24 to 27), and ultimately dissociated (R29) for detection by the mass spectrometer system at m/z 97 (S_{97SO2} in Figure 2). To mitigate interference and noise, scavenger gases (C_3F_6 in this study) were introduced to scavenge the ambient OH, creating a background signal (R23, $S_{97ScaSO2}$ in Figure 2). The ambient OH radicals signal (S_{OH}) is then determined by the subtracting $S_{97ScaSO2}$ from S_{97SO2}. The OH concentration is calculated using the following equation:

$$[OH] = \frac{1}{C_{OH}} \times \frac{S_{OH}}{S_{62}} \quad \text{(E1)}$$

Where C_{OH} represents the calibration factors of OH, and S_{62} is the signal corresponding to the reagent ion (NO_3^-). The detailed calibration procedure for OH is outlined in previous studies (Kürten et al., 2012; Zou et al., 2023).

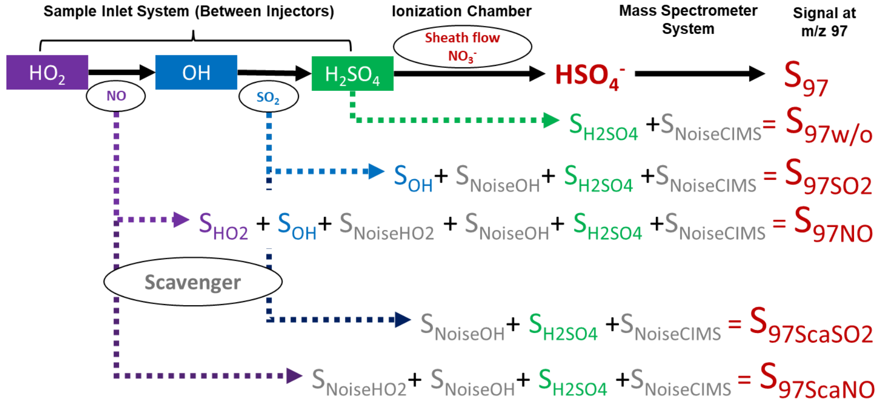

Figure 2 Flow chart depicting the relationship between measurement species and signal intensity at m/z 97 (S_{97}) with various gas injection. The color-filled grids labeled the ambient species, while oval shape label the species injected into the sample flow. Signal intensities with different gas additions to the sample flow are represented by $S_{97w/o}$, S_{97SO2}, S_{97NO}, $S_{97ScaSO2}$, and $S_{97ScaNO}$. The signals corresponding to ambient OH, HO_2, H_2SO_4 and noise from OH measurement, HO_2 measurement and the CIMS denoted as S_{OH}, S_{HO2}, S_{H2SO4}, $S_{NoiseOH}$, $S_{NoiseHO2}$ and $S_{NoiseCIMS}$, respectively.

To measure ambient HO_2, NO is injected into the sample flow, converting HO_2 to OH (R11). This converted OH then follows the same reaction pathway (R21, R24 to R27, and R29) and is measured at m/z 97 (S_{97NO} in Figure 2). Similar to the OH measurement, the background signal for HO_2 ($S_{97ScaNO}$ in Figure 2) is determined by introducing the scavenger gas. The corresponding signal for ambient HO_2 (S_{HO2} in

Figure 2) is determined by subtracting $S_{97ScaNO}$ and S_{OH} from S_{97NO}. The HO_2 concentration is calculated using a similar equation to E1, by replacing S_{OH}, and C_{OH} to S_{HO2} and C_{HO2}, respectively (E2).

$$[HO_2] = \frac{1}{C_{HO2}} \times \frac{S_{HO2}}{S_{62}} \quad \text{(E2)}$$

The procedure for determination of HO_2 calibration factor, C_{HO2}, are akin to that for C_{OH}. The calibration tube generates equal amounts of radicals (R30 in SI, $[OH]/[HO_2] = 1$), allowing for simultaneous calibration of HO_2 and OH with and without NO addition to the sample flow.

Compared to its configuration in the previous campaign (Zou et al., 2023), the PolyU-CIMS has been upgraded for simultaneous HO_2 measurements. See Figure S2, Text S2 on modification for HO_2 measurement and interference. Apart from the modifications, the PolyU-CIMS's setting, and configurations remained same as those in the previous campaign. (Table S3). With the updated configuration, the PolyU-CIMS achieved the simultaneous measurement for the three gases.

The calibration factor, detection limit and accuracy were 1.09×10^{-8} cm^{-3}, 3×10^{5} cm^{-3}, and 46% for OH; 6.01×10^{-9} cm^{-3}, 2×10^{6} cm^{-3}, and 44% for HO_2; and 1.09×10^{-8} cm^{-3}, 1×10^{5} cm^{-3}, and 40% for H_2SO_4, respectively (Table S3).

2.3 Box Model

HO_X concentrations in this study were simulated using the Framework for 0-D Atmospheric Modelling (F0AM, Wolfe et al., 2016) with the Master Chemical Mechanism (MCM) v3.3.1 (http://mcm.leeds.ac.uk/MCM), which encompasses over 6700 species and 17000 reactions. MCM v3.3.1 features a near-explicit chemical mechanism, including isoprene degradation and OH regeneration mechanisms. This mechanism has been previously employed for investigating HO_X chemistry and conducting budget analyses (Slater et al., 2020; Tan et al., 2018; Zou et al., 2023). The gas-phase chlorine chemistry described by Xu et al., (2015) and Wang et al. (2019) were included in the model (Chen et al., 2022).

In the baseline scenario, the observation data were aggregated into one-hour intervals to provide input for the model, initially constraining it without incorporating

https://doi.org/10.5194/egusphere-2024-3210
Preprint. Discussion started: 18 October 2024

observed OH and HO_2 data. For the assessment of ozone formation rates, the model was adjusted to include constraints based on the actual measured concentrations of OH and HO_2. Observed VOCs were categorized into anthropogenic origin (AVOCs), including species from petroleum gas and industrial solvent evaporation (alkenes, alkenes, benzene, and TEXs - toluene, ethylbenzene, and xylenes), and OVOCs comprising aldehydes, ketones, and acids. The sole BVOC measured in this study was isoprene. Methacrolein (MACR), a derivative of isoprene, is distinctively classified among the biogenically sourced OVOCs for further discussion. Physical processes like deposition and entrainment in the model were represented by a first-order physical loss with a 24-hour lifetime for all species (Chen et al., 2022; Wolfe et al., 2016; Zou et al., 2023). The model also included the heterogeneous uptake of HO_2 by aerosols, represented as a pseudo-first order loss (Jacob, 2000):

$$\frac{d[HO_2]}{dt} = -k_{HO_2}[HO_2] \text{ (E3)}$$

$$k_{HO_2} = \frac{V_{HO_2} \times S_a \times \gamma_{HO_2}}{4} \text{ (E4)}$$

$$v_{HO_2} = \sqrt{\frac{8RT}{\pi \times M_{HO_2}}} \text{ (E5)}$$

Here, k_{HO_2} represents the first-order loss rate coefficient of HO_2 by aerosol uptake, determined by the effective HO_2 uptake coefficient γ_{HO2} (0.1, Guo et al., 2019), the mean molecular velocity of HO_2 (v_{HO_2}), the aerosol surface area concentration (S_a) measured by the Scanning Mobility Particle Sizing (SMPS); and the molecular mass of HO_2 (M_{HO_2}= 17 g/mol). As aerosol and aqueous phase chemistry were not included in the model, it was assumed that the heterogeneous HO_2 loss would not lead to further reactions (Guo et al., 2019). For each day, a three-day spin-up was performed with constant inputs to establish stable model chemistry and reduce the uncertainty of unconstrained species.

In addition to simulating ambient concentrations, the model was also utilized to estimate an inlet interference which is the OH radicals recycled from the reaction of ambient HO_2 and NO in the inlet. The model's reaction time was set to 47 ms (matching the reaction time in the sample inlet), photolysis frequencies were set to zero, and the injection gases (SO_2) were incorporated at their injection concentrations. The rest settings and inputs remain unchanged. To access HO_2 interference caused by the ambient RO_2 conversion, the model underwent a three-days spins-up to simulate the ambient RO_2 concentration. Then by adding the injected NO and SO_2 concentration to the model, the conversion of RO_2 to OH in the inlet during HO_2 measurement mode can be estimated.

3. Results and Discussion

3.1 Results from Observations

3.1.1 Overview

Figure 3 illustrates a time series showing observed concentrations of radical and trace gases, along with meteorological parameters, from 12 November to 19 December 2022. In November, the conditions were characterised by warm temperatures ranging from 29°C to 19°C and high relative humidity averaging 86%. In contrast, December witnessed a significant decrease in temperature (ranging from 20°C to 9°C) and a reduction in relative humidity (averaging 72%). Wind speeds during the campaign were generally low, averaging 0.9 ± 0.6 m/s and typically remaining below 3.0 m/s, with higher speeds occurring towards the end of December. In November, daytime winds predominantly blew from the south, while nighttime winds came from the north. In December, northerly winds predominated both day and night. Detailed hourly wind speed and direction data are illustrated in Figure 3, and wind roses are shown in Figure S3. On days with low wind speeds (< 0.5 m/s), NO_X emissions from the G105 national highway significantly influenced chemical measurements at the monitoring site, causing morning NO levels to peak at several parts per billion (ppb). Isoprene concentrations peaked in the afternoons, ranging from 0.2 to 1.7 ppb in November and dropping to < 0.1 ppb in December. Other trace gases and particulate matter levels were higher in November than in December.

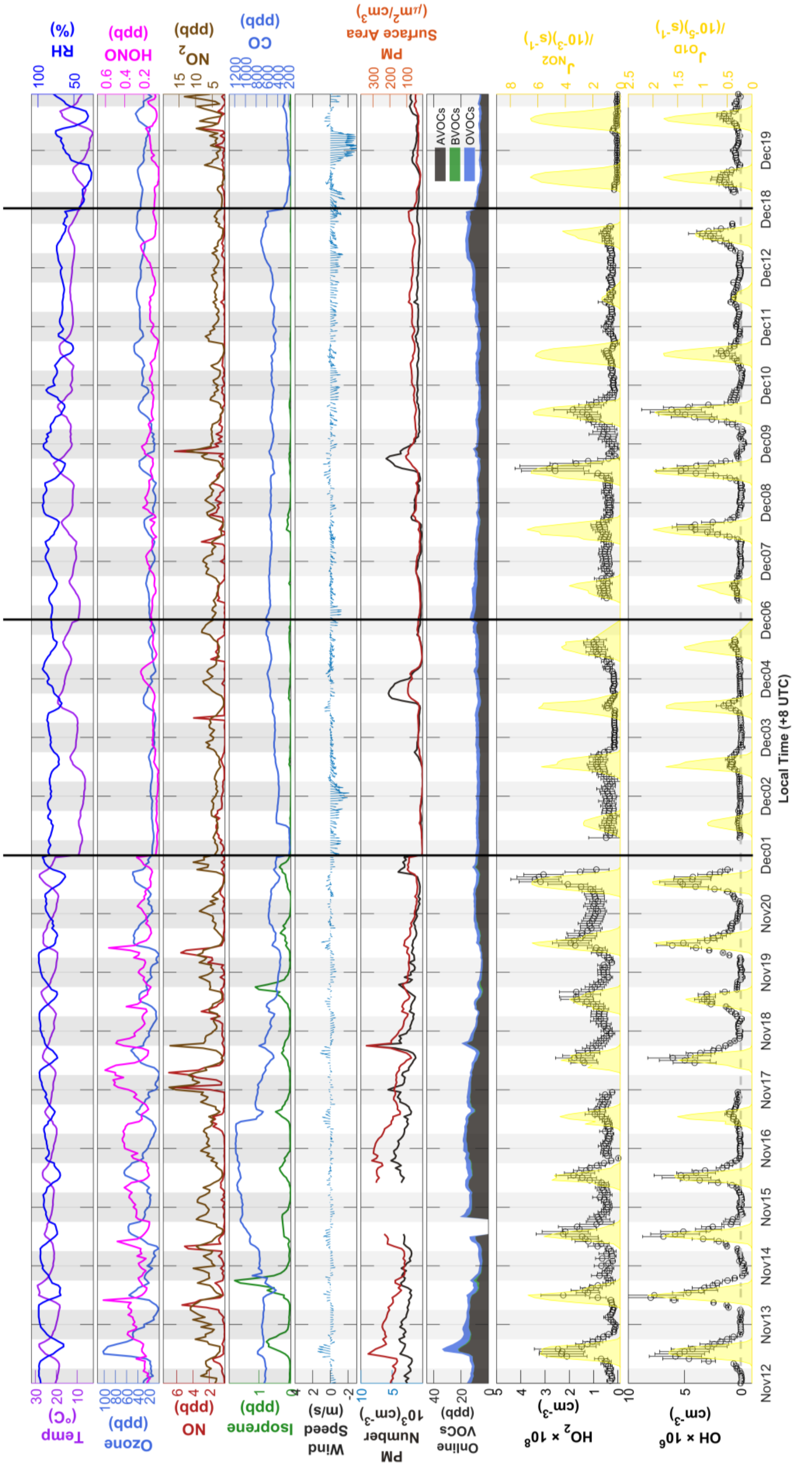
Temp (°C)
30
20
10
RH (%)
100
50
Ozone (ppb)
100
80
60
40
20
HONO (ppb)
0.6
0.4
0.2
NO (ppb)
6
4
2
NO$_2$ (ppb)
15
10
5
Isoprene (ppb)
1
0
CO (ppb)
1200
1000
800
600
400
200
Wind Speed (m/s)
4
2
0
-2
PM Number 10^3(cm^{-3})
10
5
PM Surface Area (μm^2/cm^3)
300
200
100
Online VOCs (ppb)
40
20
0
AVOCs
BVOCs
OVOCs
HO$_2$ × 10^8 (cm^{-3})
5
4
3
2
1
0
J$_{NO2}$ /(10^{-3})(s^{-1})
8
6
4
2
0
OH × 10^6 (cm^{-3})
10
5
0
J$_{O1D}$ /(10^{-5})(s^{-1})
2.5
2
1.5
1
0.5
0
Nov12
Nov13
Nov14
Nov15
Nov16
Nov17
Nov18
Nov19
Nov20
Dec01
Dec02
Dec03
Dec04
Dec06
Dec07
Dec08
Dec09
Dec10
Dec11
Dec12
Dec18
Dec19
Local Time (+8 UTC)

Figure 3 Time series of HO_2 and OH radicals between 12 November and 19 December, including measured weather conditions (temperature, RH, wind speed, and wind direction), primary sources of HO_X radicals (ozone, HONO), important sinks of the radicals (CO, isoprene, and VOCs), and photolysis frequencies of NO_2 (J_{NO2}) and ozone (J_{O1D}). Non-continuous days during the campaign are delineated by a black line. The x-axis is in local time (+8 UTC).

Throughout the campaign, the daytime concentrations of OH and HO_2 consistently exceeded detection limits and showed distinct diurnal patterns. The OH concentrations typically peaked around midday, while the HO_2 levels reached their maximum approximately one to two hours later (Figure S4). The daily maximum concentration of OH varied significantly, ranging from 8.00×10^6 cm^{-3} to nearly the detection limit of 2.54×10^5 cm^{-3}, with an average of $3.50 \pm 2.47 \times 10^6$ cm^{-3} (Table 1). Similarly, the daily maximum concentration of HO_2 varied from 3.42×10^8 cm^{-3} to 2.17×10^7 cm^{-3}, averaging $1.34 \pm 0.93 \times 10^8$ cm^{-3} (Table 1). At nighttime, while the HO_2 levels generally remained above the detection threshold, the OH concentrations frequently approached the threshold. The average nighttime concentrations were 3.92×10^7 cm^{-3} for HO_2 and 1.64×10^5 cm^{-3} for OH. We compared the observed OH and HO_2 concentrations with those reported in previous studies conducted in urban, suburban, rural forest, and coastal sites. As illustrated in Figure S5, the OH concentrations were generally lower than those found in urban settings but similar to levels observed in suburban, rural, and forest environments. This suggests a moderate level of anthropogenic activity typical of mixed forest–rural settings. In contrast, the HO_2 concentrations during these periods were significantly lower than earlier observations in rural and forest environments, likely owing to reduced photochemical activity during these specific measurement times.

Table 1 Average concentrations and standard deviation of measured species throughout the entire campaign (Total) and the selected 3 days cases from each cluster (PRD, CEC and CNC).

Species (Unit)	Total	PRD	CEC	CNC
AveMax OH_{Obs} 10^6 (cm^{-3})	3.50±2.47	6.89±1.10	4.90±1.47	5.27±0.89
OH_{Obs} 10^6 (cm^{-3})	0.93±1.49	1.60±2.18	1.36±1.61	1.19±1.77
OH_{DL} 10^6 (cm^{-3})	0.52±0.34	0.43±0.28	0.44±0.22	0.90±0.55
AveMax $HO_{2\ Obs}$ 10^8 (cm^{-3})	1.34±0.93	2.32±1.25	2.36±0.92	1.82±1.02
$HO_{2\ Obs}$ 10^8 (cm^{-3})	0.59±0.51	0.76±0.63	1.10±0.68	0.67±0.55
$HO_{2\ DL}$ 10^8 (cm^{-3})	0.19±0.11	0.17±0.10	0.25±0.08	0.26±0.15
Pressure (hpa)	995±4	992±1	992±1	995±2
Temp (°C)	16±6	23±3	23±2	14±3
RH (%)	78±15	87±11	86±10	81±9
Wind Speed (m/s)	0.9±0.7	0.5±0.3	0.6±0.3	0.9±0.5
j_{O1D} 10^{-6}(s^{-1})	3.2±5.4	3.5±6.0	3.6±5.9	4.0±6.6
j_{NO2} 10^{-3} (s^{-1})	1.3±1.9	1.3±2.1	1.4±2.0	1.6±2.3
j_{H2O2} 10^{-6} (s^{-1})	1.0±1.5	1.0±1.6	1.1±1.6	1.2±1.8
$j_{NO3\ M}$ 10^{-3} (s^{-1})	4.0±6.4	4.2±6.8	4.3±6.7	5.3±7.9
$j_{NO3\ R}$ 10^{-2} (s^{-1})	3.1±5.0	3.3±5.3	3.4±5.2	4.1±6.1
$j_{HCHO\ M}$ 10^{-6} (s^{-1})	5.2±7.9	5.5±8.5	5.6±8.3	6.4±9.5
$j_{HCHO\ R}$ 10^{-6} (s^{-1})	4.2±6.6	4.5±7.1	4.6±7.0	5.3±8.0
j_{HONO} 10^{-3}(s^{-1})	0.2±0.3	0.2±0.4	0.2±0.3	0.3±0.4
j_{H2O2} 10^{-6}(s^{-1})	1.0±1.5	1.0±1.6	1.1±1.6	1.2±1.8
HONO (ppb)	0.2±0.1	0.3±0.1	0.2±0.1	0.1±0.0
SO_2 (ppb)	0.6±0.8	0.5±0.7	0.4±0.5	0.4±0.5
NO_2 (ppb)	4.9±2.4	6.3±2.5	4.8±2.2	4.5±2.0
NO (ppb)	0.6±0.9	0.7±1.1	0.7±1.0	0.7±0.9
CO (ppb)	557±225	739±154	465±74	513±22
Ozone (ppb)	25±14	32±23	24±13	19±9
Particle Count (cm^{-3})	1629±1303	2757±567	1723±836	1329±1304
Particle Surface Area (um^2/cm^3)	86±72	186±51	84±28	48±19
MACR (ppb)	0.06±0.06	0.12±0.06	0.11±0.07	0.03±0.01
*BVOCs (ppb)	0.14±0.22	0.33±0.40	0.26±0.25	0.05±0.04
*OVOCs (ppb)	2.20±1.10	3.20±2.30	1.70±0.38	1.70±0.33
*AVOCs (ppb)	8.30±3.20	9.70±5.00	6.90±1.80	6.80±0.86

Notes: Concentrations are expressed in parts per billion (ppb) unless otherwise specified. Total VOCs concentrations are categorized by origin (AVOCs, BVOCs, and OVOCs). For the average concentration of each measured VOCs, refer to Table S4.

Figure 4 illustrates the results of the 24-hour backward trajectory analysis, revealing three distinct but sequentially occurring phases. In the initial phase (Figure 4a), air masses originated from the urban and industrial zones of the Pearl River Delta (PRD). This phase was characterised by intense photochemical activity, with ambient temperatures exceeding 20°C and relative humidity levels surpassing 70%. During this period, notably high concentrations of VOCs, ozone, and radicals were observed, with the average daily maximum concentrations of OH and HO_2 radicals reaching $6.50 \pm 1.19 \times 10^6$ cm^{-3} and $2.20 \pm 0.27 \times 10^8$ cm^{-3}, respectively. The subsequent phase was characterised by air masses originating from Central East China (CEC, Figure 4b). This phase showed reduced photochemical reactivity and lower concentrations of the measured trace gases. The average daily maximum concentrations of OH and HO_2 during this phase were 4.35 ± 2.19 × 10^6 cm^{-3} and 1.96 ± 0.90 × 10^8 cm^{-3}, respectively. The final phase was influenced by air masses from Central North China (CNC, Figure 4c), which exhibited the lowest concentrations of trace gases and the least pronounced average daily maximum concentrations in OH and HO_2 concentrations, measured at 2.23 ± 1.95 × 10^6 cm^{-3} and 7.63 ± 7.66 × 10^7 cm^{-3}, respectively. This phase coincided with an increase in cloudy days and a decrease in temperatures, indicating reduced photochemical conditions.

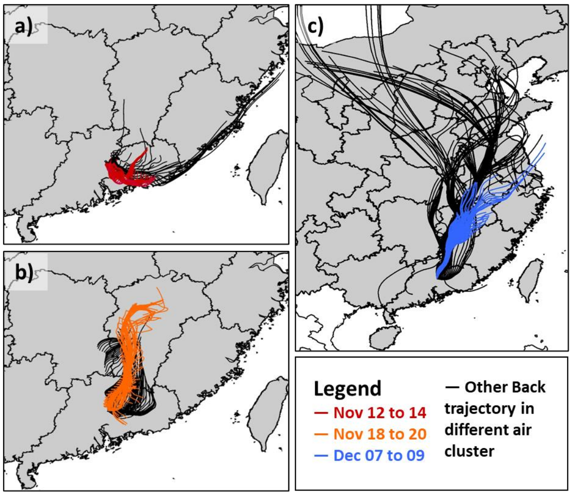

Figure 4 24-hour back trajectories for (a) Pearl River Delta (5 days), (b) Central East China (4 days), and (c) Central North China (14 days) cases. Three days selected from each cluster for model simulation are distinguished by different colours.

3.1.2 Selection of Cases

For each phase, a representative three-day period was selected for detailed analysis based on the availability of comprehensive data (colored trajectories in Figure 4). In the subsequent analysis, 'PRD,' 'CEC,' and 'CNC' refer to the selected periods corresponding to the air masses originating from these regions. The average daily maximum concentrations of OH and HO_2 radicals for these periods are presented in Table 1. The average daily max OH concentrations were 6.89 ± 1.10 × 10^6 cm^{-3} in PRD, 4.90 ± 1.47 × 10^6 cm^{-3} in CEC, and 5.27 ± 0.89 × 10^6 cm^{-3} in CNC, with a pronounce decrease from PRD to CEC (of 1.99 × 10^6 cm^{-3}). The average daily max HO_2

concentrations were 2.32 ± 1.25 × 10^8 cm^{-3} in PRD, 2.36 ± 0.92 × 10^8 cm^{-3} in CEC, and 1.82 ± 1.02 × 10^8 cm^{-3} in CNC, with a slight increase of 0.04 × 10^8 cm^{-3} from PRD to CEC and a more substantial drop of 0.54 × 10^8 cm^{-3} from CEC to CNC. These trends suggest a declining atmospheric oxidation capacity from PRD to CNC, with the factors influencing OH radicals differing significantly between PRD and CEC, and those affecting HO_2 radicals being more pronounced in CEC than CNC.

The precursor concentrations and meteorological parameters also varied across cases in terms of statistics (Table 1) and diurnal variations (Figure S6). In the PRD case, the average concentrations are characteristic of a rural environment, with AVOCs at 9.70±5.00 ppb, OVOCs at 3.20±2.30 ppb, BVOCs at 0.33±0.40 ppb, NO_2 at 6.3±2.5 ppb, and NO at 0.7±1.1 ppb. The NO concentration was affected by traffic sources as no other fresh emission source nearby and the NO diurnal variation show a morning peak in all three cases (Figure S6). In the CEC case, a general reduction in anthropogenic influence is evident. AVOCs, OVOCs and NO_2 drop significantly to 6.90±1.80 ppb, 1.70±0.38 ppb, and 4.8±2.2 ppb respectively. Meanwhile, BVOCs and NO remain close to PRD levels at 0.26±0.25 ppb and 0.7±1.0 ppb. In the CNC case, the air mass is more aged with reduced biogenic emissions, reflected in further decreases in BVOCs and NO_2 to 0.05±0.04 ppb and 4.5±2.0 ppb, respectively, due to colder weather conditions. The temperature decreased significantly from PRD to CNC, whereas the average peak photolysis frequency was comparable between PRD and CNC, as shown in Table 1.

3.2 Chemical budgets of OH and HO_2

To investigate the OH and HO_2 chemical budgets during the three distinct periods, we employed a box model constrained by observed concentrations of NO_X, VOCs, and relevant meteorological parameters in the selected cases (base scenario which OH and HO_2 concentrations were not constrained by observation here). The resulting OH and HO_2 budgets, displaying typical bell-shaped patterns, are illustrated in Figure 5. During midday (10:00–15:00), the main source of HO_2 was the recycling of RO species, with rates of 3.22 ppb h^{-1} for PRD, 2.09 ppb h^{-1} for CEC, and 1.08 ppb h^{-1} for CNC.

Additionally, HCHO photolysis contributed 0.75 ppb h^{-1}, 0.46 ppb h^{-1}, and 0.26 ppb h^{-1} for PRD, CEC, and CNC, respectively. The sinks of HO_2 varied among the cases, mainly driven by radical termination mechanisms. The rate of radical self-reactions decreased from PRD to CNC. In contrast, NO_X-radical reactions between CEC and CNC were comparable, with respective rates of 0.39 ppb h^{-1}, and 0.33 ppb h^{-1}, indicating a shift in radical termination mechanisms.

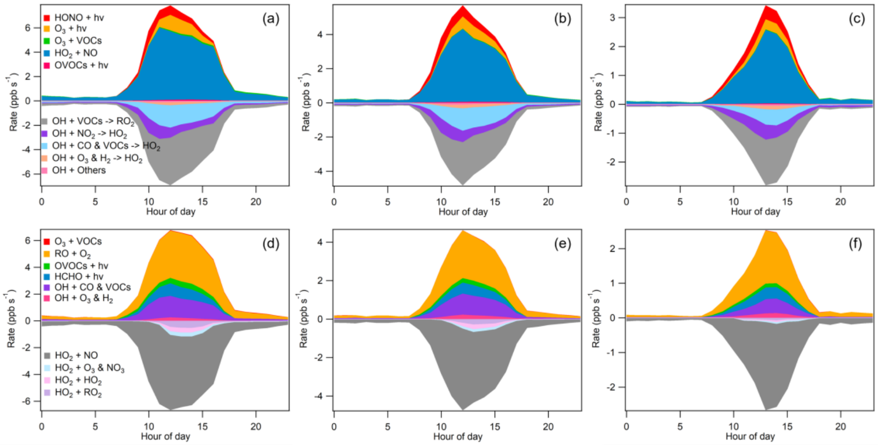

Figure 5 Chemical budgets of OH and HO_2 for PRD (a, d), CEC (b, e), and CNC (c, f) simulated using a chemical box model.

OH formation was predominantly driven by the HO_2 + NO reaction, contributing 5.18 ppb h^{-1}, 3.51 ppb h^{-1}, and 1.81 ppb h^{-1} for PRD, CEC, and CNC, respectively. Additionally, contributions from ozone photolysis and HONO increased from PRD to CEC and then to CNC, with rates of 21.4%, 22.7%, and 24.6%, respectively. The primary sinks for OH included reactions with VOCs to produce RO_2, with rates of 3.31 ppb h^{-1}, 2.02 ppb h^{-1}, and 1.13 ppb h^{-1}, and reactions with CO and other VOCs to generate HO_2, contributing 1.55 ppb h^{-1}, 1.06 ppb h^{-1}, and 0.38 ppb h^{-1} for PRD, CEC, and CNC, respectively. These findings highlight the critical role of OH + VOC reactions in the chemical budget of OH.

3.3 Model vs. Observation

To evaluate the performance of the MCM box model in simulating radical chemistry, we compared the modeled and observed concentrations of OH and HO_2

radicals. In the CNC case, the model showed good agreement with observations for both OH and HO_2 (Figures 6c and 6f). For the CEC case (Figures 6b and 6e), the model moderately overestimated both radicals. In the PRD case which is the most polluted and warmest among the three cases, the OH concentration was only slightly overestimated, but the HO_2 concentration was substantially over-predicted by the model (Figures 6a and 6d).

As mentioned in the introduction, the overestimation of OH and HO_2 radicals have been reported other studies. Griffith et al., (2013) found that while modeled OH concentrations agreed with measurements at a forested site, HO_2 concentrations were overestimated. Similarly, (Kanaya et al., 2012; Bottorff et al., 2023) reported simultaneous overestimations of OH and HO_2 in two rural sites. In our case, when the model was constrained by observed OH concentrations, the overestimation of HO_2 was resolved in the CEC case but remained largely unchanged in the PRD case (Figure S7). The exact reasons for the model's overestimation of HO_2 (in PRD and CEC) and OH (in CEC) in the remain unclear.

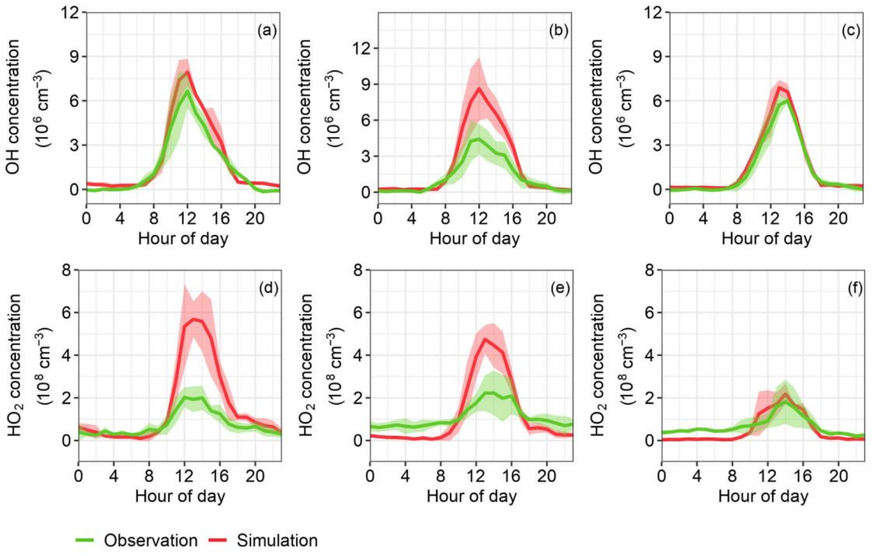

Figure 6 Average diurnal variations of OH and HO_2 for PRD (a, d), CEC (b, e), and CNC (c, f) from observational and modeling results. The solid line represents the average value, while the shaded area indicates one standard deviation. The green line represents the observational results, the

red line shows the modeled results without constraining the observed HO_2 concentration (base scenario).

4. Implication for model overestimation of HO_X

OH and HO_2 are key oxidants that determine the atmosphere's oxidative capacity. Inaccurate modelling of their sinks can lead to significant overestimation of this capacity, resulting in skewed assessments of the impact of HO_X on air pollution and climate change. This problem is particularly pronounced in the case of ozone, a widespread photochemical pollutant. To demonstrate this issue, we compared simulation results from two modelling scenarios: the first scenario was constrained by all observational parameters except OH and HO_2 (as described in section 3.2), while the second scenario included constraints from all observational parameters, including OH and HO_2 measurements.

As illustrated in Figure 7, not constraining free-radical measurement data in the chemical model (the red line) led to overestimates of ozone's photochemical production rates. In the PRD case, simulated midday O_X (O_3 + NO_2) formation rates were overestimated by 59.1% on average and 56.8% at peak values. In the CEC case, the overestimation was 98.0% on average and 91.3% at peak O_X rates, while the CNC case exhibited the smallest overestimation, 52.4% on average and 25.8% at peak values.

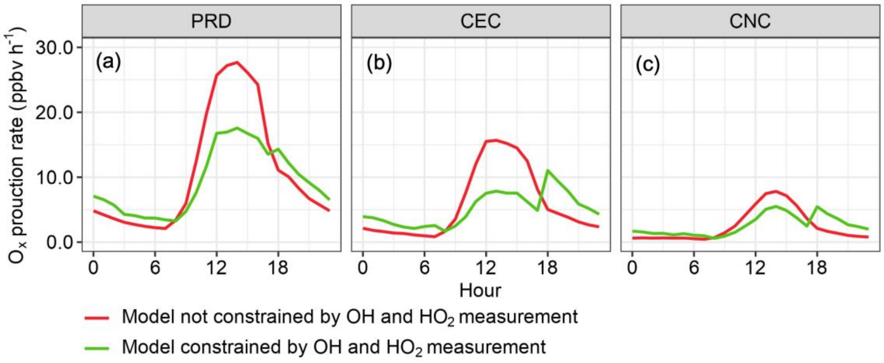

Figure 7 O_X (O_3+NO_2) photochemical production rates in three comparative cases: (a) PRD, (b) CEC, and (c) CNC. The red lines represent rates modelled with constraints on all observed data except OH and HO_2, while the green lines include constraints on all data, including OH and HO_2.

The overestimation of HO_X also significantly affected the simulated concentration of nitric acid (HNO_3), which is crucial for new particle formation and growth (Wang et al., 2020). Figure 8 illustrates that the chemical model drastically overestimated nitric acid production rates without constraints of free-radical measurements (the orange line). The midday production rates of nitric acid were overestimated by factors of 3.16, 2.02, and 3.41 in the PRD, CEC, and CNC cases, respectively. Such overestimations can considerably impact assessments of air pollution and climate change.

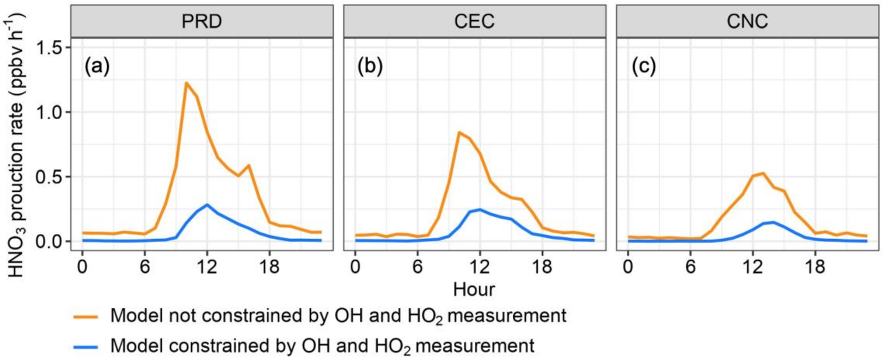

Figure 8 Modelled HNO_3 concentrations in three comparative cases: (a) PRD, (b) CEC, and (c) CNC. The red lines represent rates modelled with constraints on all observed data except OH and HO_2, while the green lines include constraints on all data, including OH and HO_2.

5. Conclusion

HO_2 and OH concentrations were measured using a chemical ionization mass spectrometer at a subtropical rural site in southern China from 12 November to 19 December 2022. The measurements indicated generally lower concentrations of OH and HO_2 than those observed in previous studies at various sites. Backward trajectory analysis revealed three distinct phases characterised by sequentially decreasing pollution levels and temperatures. During the cold, clean period, model simulations closely matched the observed OH and HO_2 concentrations. However, during the warm, polluted period, the models overestimated both radicals. The over-prediction of HO_X resulted in significant overestimations of the production rates of other secondary pollutants such as ozone and nitric acid at the site. This study provides additional evidence for current incomplete understanding of the HO_X sources or sinks and calls for more research to resolve the model–observation mismatch found in this work and previous studies. It is critical to evaluate the capability of OH and HO_2 simulations in major chemical transport models and Earth system models as inaccurate simulations of OH and HO_2 may misguide the development of air pollution and global warming control strategies.

Data availability. All of the data used to produce this paper can be obtained by contacting Tao Wang (tao.wang@polyu.edu.hk).

Supplement. The online supplement for this article is available at:

Author contributions. TW conceived the HO_x research. TW, XW and YZ planned and organized the overall field campaign at Conghua. ZZ conducted the OH measurements using CIMS, with contributions from TW and WS, QC, and SH. XF, ZR, XL, AG, QW, CP, and XT performed the JNO_2 VOCs and OVOCs measurements. ZZ performed the chemical box modelling with contributions from TC and QC. TC, ZZ, and TW analysed the data and interpreted the result (ZZ analysed the time series and diurnal variations of observation data; TC interpreted the results of box model, investigated the missing sources; TW supervised and guided these processes). TC, ZZ, and TW wrote the paper. All of the authors reviewed and commented on the paper.

Competing interests. One author (Tao Wang) is a member of the editorial board of Atmospheric Chemistry and Physics. The authors have no other competing interests to declare.

Acknowledgments

We thank David Tanner, Dr. Wei Pu, and Dr. Weihao Wang for developing the PolyU-CIMS. We are also grateful to the Guangzhou Institute of Geochemistry, Chinese Academy of Sciences, for providing access to its station and data on trace gases.

Financial support.

This research was financially supported by the Hong Kong Research Grants Council (T24-504/17-N and 15223221 to Tao Wang), the National Science Foundation of China

(42293322 to Tao Wang), and The Hong Kong Polytechnic University Postdoc Matching Fund Scheme (P0043403 to Tianshu Chen).

Reference

Berresheim, H., Elste, T., Tremmel, H. G., Allen, A. G., Hansson, H.-C., Rosman, K., Dal Maso, M., Mäkelä, J. M., Kulmala, M., and O'Dowd, C. D.: Gas-aerosol relationships of H_2SO_4, MSA, and OH: Observations in the coastal marine boundary layer at Mace Head, Ireland, Journal of Geophysical Research: Atmospheres, 107, PAR 5-1-PAR 5-12, https://doi.org/10.1029/2000JD000229, 2002.

Bottorff, B., Lew, M. M., Woo, Y., Rickly, P., Rollings, M. D., Deming, B., Anderson, D. C., Wood, E., Alwe, H. D., Millet, D. B., Weinheimer, A., Tyndall, G., Ortega, J., Dusanter, S., Leonardis, T., Flynn, J., Erickson, M., Alvarez, S., Rivera-Rios, J. C., Shutter, J. D., Keutsch, F., Helmig, D., Wang, W., Allen, H. M., Slade, J. H., Shepson, P. B., Bertman, S., and Stevens, P. S.: OH, HO_2, and RO_2 radical chemistry in a rural forest environment: measurements, model comparisons, and evidence of a missing radical sink, Atmospheric Chemistry and Physics, 23, 10287–10311, https://doi.org/10.5194/acp-23-10287-2023, 2023.

Carslaw, N., Creasey, D. J., Heard, D. E., Lewis, A. C., McQuaid, J. B., Pilling, M. J., Monks, P. S., Bandy, B. J., and Penkett, S. A.: Modeling OH, HO_2, and RO_2 radicals in the marine boundary layer: 1. Model construction and comparison with field measurements, J. Geophys. Res., 104, 30241–30255, https://doi.org/10.1029/1999JD900783, 1999.

Chen, Q., Xia, M., Peng, X., Yu, C., Sun, P., Li, Y., Liu, Y., Xu, Z., Xu, Z., Wu, R., Nie, W., Ding, A., Zhao, Y., and Wang, T.: Large Daytime Molecular Chlorine Missing Source at a Suburban Site in East China, JGR Atmospheres, 127, https://doi.org/10.1029/2021JD035796, 2022.

Edwards, G. D., Cantrell, C. A., Stephens, S., Hill, B., Goyea, O., Shetter, R. E., Mauldin, R. L., Kosciuch, E., Tanner, D. J., and Eisele, F. L.: Chemical Ionization Mass Spectrometer Instrument for the Measurement of Tropospheric HO_2 and RO_2, Anal. Chem., 75, 5317–5327, https://doi.org/10.1021/ac034402b, 2003.

Eisele, F. L. and Tanner, D. J.: Ion-assisted tropospheric OH measurements, J. Geophys. Res., 96, 9295, https://doi.org/10.1029/91JD00198, 1991.

Eisele, F. L. and Tanner, D. J.: Measurement of the gas phase concentration of H_2SO_4 and methane sulfonic acid and estimates of H_2SO_4 production and loss in the atmosphere, Journal of Geophysical Research: Atmospheres, 98, 9001–9010, https://doi.org/10.1029/93JD00031, 1993.

Feiner, P. A., Brune, W. H., Miller, D. O., Zhang, L., Cohen, R. C., Romer, P. S., Goldstein, A. H., Keutsch, F. N., Skog, K. M., Wennberg, P. O., Nguyen, T. B., Teng, A. P., DeGouw, J., Koss, A., Wild, R. J., Brown, S. S., Guenther, A., Edgerton, E., Baumann, K., and Fry, J. L.: Testing Atmospheric Oxidation in an Alabama Forest, Journal of the Atmospheric Sciences, 73, 4699–

4710, https://doi.org/10.1175/JAS-D-16-0044.1, 2016.

Fuchs, H., Bohn, B., Hofzumahaus, A., Holland, F., Lu, K. D., Nehr, S., Rohrer, F., and Wahner, A.: Detection of HO_2 by laser-induced fluorescence: calibration and interferences from RO_2 radicals, Atmospheric Measurement Techniques, 4, 1209–1225, https://doi.org/10.5194/amt-4-1209-2011, 2011.

Griffith, S. M., Hansen, R. F., Dusanter, S., Stevens, P. S., Alaghmand, M., Bertman, S. B., Carroll, M. A., Erickson, M., Galloway, M., Grossberg, N., Hottle, J., Hou, J., Jobson, B. T., Kammrath, A., Keutsch, F. N., Lefer, B. L., Mielke, L. H., O'Brien, A., Shepson, P. B., Thurlow, M., Wallace, W., Zhang, N., and Zhou, X. L.: OH and HO_2 radical chemistry during PROPHET 2008 and CABINEX 2009 - Part 1: Measurements and model comparison, Atmospheric Chemistry and Physics, 13, 5403–5423, https://doi.org/10.5194/acp-13-5403-2013, 2013.

Guo, J., Wang, Z., Tao Wang, and Zhang, X.: Theoretical evaluation of different factors affecting the HO_2 uptake coefficient driven by aqueous-phase first-order loss reaction, Science of The Total Environment, 683, 146–153, https://doi.org/10.1016/j.scitotenv.2019.05.237, 2019.

Hansen, R. F., Griffith, S. M., Dusanter, S., Rickly, P. S., Stevens, P. S., Bertman, S. B., Carroll, M. A., Erickson, M. H., Flynn, J. H., Grossberg, N., Jobson, B. T., Lefer, B. L., and Wallace, H. W.: Measurements of total hydroxyl radical reactivity during CABINEX 2009 – Part 1: field measurements, Atmos. Chem. Phys., 14, 2923–2937, https://doi.org/10.5194/acp-14-2923-2014, 2014.

Heard, D. E. and Pilling, M. J.: Measurement of OH and HO_2 in the Troposphere, Chem. Rev., 103, 5163–5198, https://doi.org/10.1021/cr020522s, 2003.

Hens, K., Novelli, A., Martinez, M., Auld, J., Axinte, R., Bohn, B., Fischer, H., Keronen, P., Kubistin, D., Nölscher, A. C., Oswald, R., Paasonen, P., Petäjä, T., Regelin, E., Sander, R., Sinha, V., Sipilä, M., Taraborrelli, D., Tatum Ernest, C., Williams, J., Lelieveld, J., and Harder, H.: Observation and modelling of HO_x radicals in a boreal forest, Atmospheric Chemistry and Physics, 14, 8723–8747, https://doi.org/10.5194/acp-14-8723-2014, 2014.

Hofzumahaus, A., Rohrer, F., Lu, K., Bohn, B., Brauers, T., Chang, C.-C., Fuchs, H., Holland, F., Kita, K., Kondo, Y., Li, X., Lou, S., Shao, M., Zeng, L., Wahner, A., and Zhang, Y.: Amplified Trace Gas Removal in the Troposphere, Science, 324, 1702–1704, https://doi.org/10.1126/science.1164566, 2009.

Jacob, D.: Heterogeneous chemistry and tropospheric ozone, Atmospheric Environment, 34, 2131–2159, https://doi.org/10.1016/S1352-2310(99)00462-8, 2000.

Jeong, D., Seco, R., Emmons, L., Schwantes, R., Liu, Y., McKinney, K. A., Martin, S. T., Keutsch, F. N., Gu, D., Guenther, A. B., Vega, O., Tota, J., Souza, R. A. F., Springston, S. R., Watson, T. B., and Kim, S.: Reconciling Observed and Predicted Tropical Rainforest OH Concentrations, JGR Atmospheres, 127, https://doi.org/10.1029/2020JD032901, 2022.

Kanaya, Y., Cao, R., Kato, S., Miyakawa, Y., Kajii, Y., Tanimoto, H., Yokouchi, Y., Mochida, M., Kawamura, K., and Akimoto, H.: Chemistry of OH and HO_2 radicals observed at Rishiri Island, Japan, in September 2003: Missing daytime sink of HO_2 and positive nighttime correlations with monoterpenes, J. Geophys. Res., 112, D11308, https://doi.org/10.1029/2006JD007987, 2007.

Kanaya, Y., Hofzumahaus, A., Dorn, H.-P., Brauers, T., Fuchs, H., Holland, F., Rohrer, F., Bohn, B., Tillmann, R., Wegener, R., Wahner, A., Kajii, Y., Miyamoto, K., Nishida, S., Watanabe, K., Yoshino, A., Kubistin, D., Martinez, M., Rudolf, M., Harder, H., Berresheim, H., Elste, T., Plass-Dülmer, C., Stange, G., Kleffmann, J., Elshorbany, Y., and Schurath, U.: Comparisons of observed and modeled OH and HO_2 concentrations during the ambient measurement period of the HO_xComp field campaign, Atmospheric Chemistry and Physics, 12, 2567–2585, https://doi.org/10.5194/acp-12-2567-2012, 2012.

Kim, S., Wolfe, G. M., Mauldin, L., Cantrell, C., Guenther, A., Karl, T., Turnipseed, A., Greenberg, J., Hall, S. R., Ullmann, K., Apel, E., Hornbrook, R., Kajii, Y., Nakashima, Y., Keutsch, F. N., DiGangi, J. P., Henry, S. B., Kaser, L., Schnitzhofer, R., Graus, M., Hansel, A., Zheng, W., and Flocke, F. F.: Evaluation of HO_x sources and cycling using measurement-constrained model calculations in a 2-methyl-3-butene-2-ol (MBO) and monoterpene (MT) dominated ecosystem, Atmospheric Chemistry and Physics, 13, 2031–2044, https://doi.org/10.5194/acp-13-2031-2013, 2013.

Kürten, A., Rondo, L., Ehrhart, S., and Curtius, J.: Calibration of a Chemical Ionization Mass Spectrometer for the Measurement of Gaseous Sulfuric Acid, J. Phys. Chem. A, 116, 6375–6386, https://doi.org/10.1021/jp212123n, 2012.

Lelieveld, J., Butler, T. M., Crowley, J. N., Dillon, T. J., Fischer, H., Ganzeveld, L., Harder, H., Lawrence, M. G., Martinez, M., Taraborrelli, D., and Williams, J.: Atmospheric oxidation capacity sustained by a tropical forest, Nature, 452, 737–740, https://doi.org/10.1038/nature06870, 2008.

Lew, M. M., Rickly, P. S., Bottorff, B. P., Reidy, E., Sklaveniti, S., Léonardis, T., Locoge, N., Dusanter, S., Kundu, S., Wood, E., and Stevens, P. S.: OH and HO_2 radical chemistry in a midlatitude forest: measurements and model comparisons, Atmospheric Chemistry and Physics, 20, 9209–9230, https://doi.org/10.5194/acp-20-9209-2020, 2020.

Lou, S., Holland, F., Rohrer, F., Lu, K., Bohn, B., Brauers, T., Chang, C. C., Fuchs, H., Häseler, R., Kita, K., Kondo, Y., Li, X., Shao, M., Zeng, L., Wahner, A., Zhang, Y., Wang, W., and Hofzumahaus, A.: Atmospheric OH reactivities in the Pearl River Delta – China in summer 2006: measurement and model results, Atmos. Chem. Phys., 10, 11243–11260, https://doi.org/10.5194/acp-10-11243-2010, 2010.

Ma, X., Tan, Z., Lu, K., Yang, X., Liu, Y., Li, S., Li, X., Chen, S., Novelli, A., Cho, C., Zeng, L., Wahner, A., and Zhang, Y.: Winter photochemistry in Beijing: Observation and model simulation of OH and HO2 radicals at an urban site, Science of The Total Environment, 685, 85–95, https://doi.org/10.1016/j.scitotenv.2019.05.329, 2019.

Ma, X., Tan, Z., Lu, K., Yang, X., Chen, X., Wang, H., Chen, S., Fang, X., Li, S., Li, X., Liu, J., Liu, Y., Lou, S., Qiu, W., Wang, H., Zeng, L., and Zhang, Y.: OH and HO_2 radical chemistry at a suburban site during the EXPLORE-YRD campaign in 2018, Atmospheric Chemistry and Physics, 22, 7005–7028, https://doi.org/10.5194/acp-22-7005-2022, 2022.

Mallik, C., Tomsche, L., Bourtsoukidis, E., Crowley, J. N., Derstroff, B., Fischer, H., Hafermann, S., Hüser, I., Javed, U., Keßel, S., Lelieveld, J., Martinez, M., Meusel, H., Novelli, A., Phillips, G. J., Pozzer, A., Reiffs, A., Sander, R., Taraborrelli, D., Sauvage, C., Schuladen, J., Su, H., Williams, J., and Harder, H.: Oxidation processes in the eastern Mediterranean atmosphere: evidence from the modelling of HO_x measurements over Cyprus, Atmospheric Chemistry and Physics, 18, 10825–10847, https://doi.org/10.5194/acp-18-10825-2018, 2018.

Mao, J., Ren, X., Zhang, L., Van Duin, D. M., Cohen, R. C., Park, J.-H., Goldstein, A. H., Paulot, F., Beaver, M. R., Crounse, J. D., Wennberg, P. O., DiGangi, J. P., Henry, S. B., Keutsch, F. N., Park, C., Schade, G. W., Wolfe, G. M., Thornton, J. A., and Brune, W. H.: Insights into hydroxyl measurements and atmospheric oxidation in a California forest, Atmos. Chem. Phys., 12, 8009–8020, https://doi.org/10.5194/acp-12-8009-2012, 2012.

Mauldin III, R. L., Kosciuch, E., Henry, B., Eisele, F. L., Shetter, R., Lefer, B., Chen, G., Davis, D., Huey, G., and Tanner, D.: Measurements of OH, HO_2+RO_2, H_2SO_4, and MSA at the South Pole during ISCAT 2000, Atmospheric Environment, 38, 5423–5437, https://doi.org/10.1016/j.atmosenv.2004.06.031, 2004.

Muller, J. B. A., Elste, T., Plass-Dülmer, C., Stange, G., Holla, R., Claude, A., Englert, J., Gilge, S., and Kubistin, D.: A novel semi-direct method to measure OH reactivity by chemical ionization mass spectrometry (CIMS), Atmos. Meas. Tech., 11, 4413–4433, https://doi.org/10.5194/amt-11-4413-2018, 2018.

Novelli, A., Hens, K., Tatum Ernest, C., Kubistin, D., Regelin, E., Elste, T., Plass-Dülmer, C., Martinez, M., Lelieveld, J., and Harder, H.: Characterisation of an inlet pre-injector laser-induced fluorescence instrument for the measurement of atmospheric hydroxyl radicals, Atmos. Meas. Tech., 7, 3413–3430, https://doi.org/10.5194/amt-7-3413-2014, 2014.

Novelli, A., Vereecken, L., Bohn, B., Dorn, H.-P., Gkatzelis, G. I., Hofzumahaus, A., Holland, F., Reimer, D., Rohrer, F., Rosanka, S., Taraborrelli, D., Tillmann, R., Wegener, R., Yu, Z., Kiendler-Scharr, A., Wahner, A., and Fuchs, H.: Importance of isomerization reactions for OH radical regeneration from the photo-oxidation of isoprene investigated in the atmospheric simulation chamber SAPHIR, Atmos. Chem. Phys., 20, 3333–3355, https://doi.org/10.5194/acp-20-3333-2020, 2020.

Sjostedt, S. J., Huey, L. G., Tanner, D. J., Peischl, J., Chen, G., Dibb, J. E., Lefer, B., Hutterli, M. A., Beyersdorf, A. J., Blake, N. J., Blake, D. R., Sueper, D., Ryerson, T., Burkhart, J., and Stohl, A.: Observations of hydroxyl and the sum of peroxy radicals at Summit, Greenland during summer 2003, Atmospheric Environment, 41, 5122–5137, https://doi.org/10.1016/j.atmosenv.2006.06.065, 2007.

Slater, E. J., Whalley, L. K., Woodward-Massey, R., Ye, C., Lee, J. D., Squires, F., Hopkins, J. R., Dunmore, R. E., Shaw, M., Hamilton, J. F., Lewis, A. C., Crilley, L. R., Kramer, L., Bloss, W., Vu, T., Sun, Y., Xu, W., Yue, S., Ren, L., Acton, W. J. F., Hewitt, C. N., Wang, X., Fu, P., and Heard, D. E.: Elevated levels of OH observed in haze events during wintertime in central Beijing, Atmospheric Chemistry and Physics, 20, 14847–14871, https://doi.org/10.5194/acp-20-14847-2020, 2020.

Stone, D., Whalley, L. K., and Heard, D. E.: Tropospheric OH and HO_2 radicals: field measurements and model comparisons, Chem. Soc. Rev., 41, 6348, https://doi.org/10.1039/c2cs35140d, 2012.

Tan, D., Faloona, I., Simpas, J. B., Brune, W., Shepson, P. B., Couch, T. L., Sumner, A. L., Carroll, M. A., Thornberry, T., Apel, E., Riemer, D., and Stockwell, W.: HO_x budgets in a deciduous forest: Results from the PROPHET summer 1998 campaign, J. Geophys. Res., 106, 24407–24427, https://doi.org/10.1029/2001JD900016, 2001.

Tan, Z., Fuchs, H., Lu, K., Hofzumahaus, A., Bohn, B., Broch, S., Dong, H., Gomm, S., Häseler, R., He, L., Holland, F., Li, X., Liu, Y., Lu, S., Rohrer, F., Shao, M., Wang, B., Wang, M., Wu, Y., Zeng, L., Zhang, Y., Wahner, A., and Zhang, Y.: Radical chemistry at a rural site (Wangdu) in the North China Plain: observation and model calculations of OH, HO_2 and RO_2 radicals, Atmospheric Chemistry and Physics, 17, 663–690, https://doi.org/10.5194/acp-17-663-2017, 2017.

Tan, Z., Rohrer, F., Lu, K., Ma, X., Bohn, B., Broch, S., Dong, H., Fuchs, H., Gkatzelis, G. I., Hofzumahaus, A., Holland, F., Li, X., Liu, Y., Liu, Y., Novelli, A., Shao, M., Wang, H., Wu, Y., Zeng, L., Hu, M., Kiendler-Scharr, A., Wahner, A., and Zhang, Y.: Wintertime photochemistry in Beijing: observations of RO_x radical concentrations in the North China Plain during the BEST-ONE campaign, Atmospheric Chemistry and Physics, 18, 12391–12411, https://doi.org/10.5194/acp-18-12391-2018, 2018.

Tan, Z., Lu, K., Hofzumahaus, A., Fuchs, H., Bohn, B., Holland, F., Liu, Y., Rohrer, F., Shao, M., Sun, K., Wu, Y., Zeng, L., Zhang, Y., Zou, Q., Kiendler-Scharr, A., Wahner, A., and Zhang, Y.: Experimental budgets of OH, HO_2, and RO_2 radicals and implications for ozone formation in the Pearl River Delta in China 2014, Atmospheric Chemistry and Physics, 19, 7129–7150, https://doi.org/10.5194/acp-19-7129-2019, 2019.

Tanner, D. J. and Eisele, F. L.: Present OH measurement limits and associated uncertainties, J. Geophys. Res., 100, 2883, https://doi.org/10.1029/94JD02609, 1995.

Tanner, D. J., Jefferson, A., and Eisele, F. L.: Selected ion chemical ionization mass spectrometric measurement of OH, J. Geophys. Res., 102, 6415–6425, https://doi.org/10.1029/96JD03919, 1997.

Thames, A. B., Brune, W. H., Miller, D. O., Allen, H. M., Apel, E. C., Blake, D. R., Bui, T. P., Commane, R., Crounse, J. D., Daube, B. C., Diskin, G. S., DiGangi, J. P., Elkins, J. W., Hall, S. R., Hanisco, T. F., Hannun, R. A., Hintsa, E., Hornbrook, R. S., Kim, M. J., McKain, K., Moore, F. L., Nicely, J. M., Peischl, J., Ryerson, T. B., St. Clair, J. M., Sweeney, C., Teng, A., Thompson, C. R., Ullmann, K., Wennberg, P. O., and Wolfe, G. M.: Missing OH reactivity in the global marine boundary layer, Atmospheric Chemistry and Physics, 20, 4013–4029, https://doi.org/10.5194/acp-20-4013-2020, 2020.

Wang, M., Kong, W., Marten, R., He, X.-C., Chen, D., Pfeifer, J., Heitto, A., Kontkanen, J., Dada, L., Kürten, A., Yli-Juuti, T., Manninen, H. E., Amanatidis, S., Amorim, A., Baalbaki, R., Baccarini, A., Bell, D. M., Bertozzi, B., Bräkling, S., Brilke, S., Murillo, L. C., Chiu, R., Chu, B., De Menezes, L.-P., Duplissy, J., Finkenzeller, H., Carracedo, L. G., Granzin, M., Guida, R., Hansel, A., Hofbauer, V., Krechmer, J., Lehtipalo, K., Lamkaddam, H., Lampimäki, M., Lee, C. P., Makhmutov, V., Marie, G., Mathot, S., Mauldin, R. L., Mentler, B., Müller, T., Onnela, A., Partoll, E., Petäjä, T., Philippov, M., Pospisilova, V., Ranjithkumar, A., Rissanen, M., Rörup, B., Scholz, W., Shen, J., Simon, M., Sipilä, M., Steiner, G., Stolzenburg, D., Tham, Y. J., Tomé, A., Wagner, A. C., Wang, D. S., Wang, Y., Weber, S. K., Winkler, P. M., Wlasits, P. J., Wu, Y., Xiao, M., Ye, Q., Zauner-Wieczorek, M., Zhou, X., Volkamer, R., Riipinen, I., Dommen, J., Curtius, J., Baltensperger, U., Kulmala, M., Worsnop, D. R., Kirkby, J., Seinfeld, J. H., El-Haddad, I., Flagan, R. C., and Donahue, N. M.: Rapid growth of new atmospheric particles by nitric acid and ammonia condensation, Nature, 581, 184–189, https://doi.org/10.1038/s41586-020-2270-4, 2020.

Wang, X., Jacob, D. J., Eastham, S. D., Sulprizio, M. P., Zhu, L., Chen, Q., Alexander, B., Sherwen, T., Evans, M. J., Lee, B. H., Haskins, J. D., Lopez-Hilfiker, F. D., Thornton, J. A., Huey, G. L., and Liao, H.: The role of chlorine in global tropospheric chemistry, Atmospheric Chemistry and Physics, 19, 3981–4003, https://doi.org/10.5194/acp-19-3981-2019, 2019.

Wennberg, P. O., Bates, K. H., Crounse, J. D., Dodson, L. G., McVay, R. C., Mertens, L. A., Nguyen, T. B., Praske, E., Schwantes, R. H., Smarte, M. D., St Clair, J. M., Teng, A. P., Zhang, X., and Seinfeld, J. H.: Gas-Phase Reactions of Isoprene and Its Major Oxidation Products, Chem. Rev., 118, 3337–3390, https://doi.org/10.1021/acs.chemrev.7b00439, 2018.

Whalley, L. K., Edwards, P. M., Furneaux, K. L., Goddard, A., Ingham, T., Evans, M. J., Stone, D., Hopkins, J. R., Jones, C. E., Karunaharan, A., Lee, J. D., Lewis, A. C., Monks, P. S., Moller, S. J., and Heard, D. E.: Quantifying the magnitude of a missing hydroxyl radical source in a tropical rainforest, Atmos. Chem. Phys., 11, 7223–7233, https://doi.org/10.5194/acp-11-7223-2011, 2011.

Wolfe, G. M., Marvin, M. R., Roberts, S. J., Travis, K. R., and Liao, J.: The Framework for 0-D Atmospheric Modeling (F0AM) v3.1, Geosci. Model Dev., 9, 3309–3319, https://doi.org/10.5194/gmd-9-3309-2016, 2016.

Woodward-Massey, R., Slater, E. J., Alen, J., Ingham, T., Cryer, D. R., Stimpson, L. M., Ye, C., Seakins, P. W., Whalley, L. K., and Heard, D. E.: Implementation of a chemical background method for atmospheric OH measurements by laser-induced fluorescence: characterisation and observations from the UK and China, Atmospheric Measurement Techniques, 13, 3119–3146, https://doi.org/10.5194/amt-13-3119-2020, 2020.

Xu, Z., Xue, L., Wang, T., Xia, T., Gao, Y., Louie, P. K. K., and Luk, C. W. Y.: Measurements of

Peroxyacetyl Nitrate at a Background Site in the Pearl River Delta Region: Production Efficiency and Regional Transport, Aerosol Air Qual. Res., 15, 833–841, https://doi.org/10.4209/aaqr.2014.11.0275, 2015.

Yang, X., Lu, K., Ma, X., Liu, Y., Wang, H., Hu, R., Li, X., Lou, S., Chen, S., Dong, H., Wang, F., Wang, Y., Zhang, G., Li, S., Yang, S., Yang, Y., Kuang, C., Tan, Z., Chen, X., Qiu, P., Zeng, L., Xie, P., and Zhang, Y.: Observations and modeling of OH and HO2 radicals in Chengdu, China in summer 2019, Science of The Total Environment, 772, 144829, https://doi.org/10.1016/j.scitotenv.2020.144829, 2021.

Yang, X., Lu, K., Ma, X., Gao, Y., Tan, Z., Wang, H., Chen, X., Li, X., Huang, X., He, L., Tang, M., Zhu, B., Chen, S., Dong, H., Zeng, L., and Zhang, Y.: Radical chemistry in the Pearl River Delta: observations and modeling of OH and HO_2 radicals in Shenzhen in 2018, Atmospheric Chemistry and Physics, 22, 12525–12542, https://doi.org/10.5194/acp-22-12525-2022, 2022.

Yang, Y., Shao, M., Wang, X., Nölscher, A. C., Kessel, S., Guenther, A., and Williams, J.: Towards a quantitative understanding of total OH reactivity: A review, Atmospheric Environment, 134, 147–161, https://doi.org/10.1016/j.atmosenv.2016.03.010, 2016.

Zou, Z., Chen, Q., Xia, M., Yuan, Q., Chen, Y., Wang, Y., Xiong, E., Wang, Z., and Wang, T.: OH measurements in the coastal atmosphere of South China: possible missing OH sinks in aged air masses, Atmospheric Chemistry and Physics, 23, 7057–7074, https://doi.org/10.5194/acp-23-7057-2023, 2023.